Thermal and Pressure Ionization in Warm, Dense MgSiO$_3$ Studied with First-Principles Computer Simulations

Felipe González-Cataldo[1, a)] and Burkhard Militzer[1, 2]

[1)]*Department of Earth and Planetary Science, University of California, Berkeley, California 94720, USA*
[2)]*Department of Astronomy, University of California, Berkeley, California 94720, USA*

[a)]*Corresponding author: f_gonzalez@berkeley.edu*

Abstract. Using path integral Monte Carlo and density functional molecular dynamics (DFT-MD) simulations, we study the properties of MgSiO$_3$ enstatite in the regime of warm dense matter. We generate a consistent equation of state (EOS) that spans across a wide range of temperatures and densities (10^4–10^7 K and 6.42–64.16 g cm^{-3}). We derive the shock Hugoniot curve, that is in good agreement with the experiments. We identify the boundary between the regimes of thermal ionization and pressure ionization by locating where the internal energy at constant temperature attains a minimum as a function of density or pressure. At low density, the internal energy decreases with increasing density as the weight of free states changes. Thermal ionization dominates. Conversely, at high density, in the regime of pressure ionization, the internal energy increases with density. We determine the boundary between the two regimes and show that the compression maximum along the shock Hugoniot curve occurs because K shell electrons become thermally ionized rather than pressure ionized.

INTRODUCTION

Enstatite, MgSiO$_3$, is one of the most abundant minerals on Earth's crust and one of the few silicate minerals that has been observed in crystalline form outside the Solar System [1]. Therefore, it has been identified as one the primary building blocks of planetary formation [2, 3] and it is commonly used as a representative mantle material in exoplanet modeling [2, 4, 5, 6]. The equation of state (EOS) of silicate materials at high pressures and temperatures is fundamental to develop models of planetary formation [7] and to interpret results from shock compression experiments [8]. In planetary collision events, for example, the amount of heat generated during the shock can be sufficient to melt and even vaporize these minerals [9], and an accurate EOS is needed to describe these processes quantitatively. On the other hand, precise first-principles computer simulations of silicates can guide the design of inertial confinement fusion (ICF) experiments [10, 11, 12] under conditions where the K and L shell electrons are gradually ionized, which is challenging to predict accurately with analytical EOS models.

The properties of the liquid phase of MgSiO$_3$ at high pressure have recently been explored in laser-driven shock compression experiments [3, 8, 13], and suggest a metallic-like behavior over a wide range of pressure-temperature conditions. Similar findings were reported with first-principles calculations [14] that demonstrated that super-Earth planets can generate magnetic fields within their mantles.

In this work, we combine path integral Monte Carlo (PIMC) and density functional theory molecular dynamics (DFT-MD) simulations to study the ionization in warm, dense MgSiO$_3$. We distinguish the regimes of thermal ionization and pressure ionization, and show that the shock Hugoniot curve crosses from one regime into the other. The compression maximum along the Hugoniot curve is found to fall within the regime of thermal ionization. The K shell electrons of all three nuclei contribute to the compression maximum.

METHODOLOGY

Rigorous discussions of the PIMC [15, 16, 17, 18] and DFT-MD [19, 20, 21] methods have been provided in previous works, and the details of our simulations have been presented in some of our previous publications [22, 23]. Here we summarize the methods and provide the simulation parameters specific to simulations of MgSiO$_3$ plasma. The general idea of our approach is to perform simulations along isochores at high temperatures ($T \geqslant 10^6$ K) using PIMC and at low temperatures ($T \leqslant 10^6$ K) using DFT-MD simulations. We find the two methods produce consistent results at overlapping temperatures [12, 24].

For PIMC simulations, we use the CUPID code [25, 26, 27] with Hartree-Fock nodes [28, 29, 30]. For DFT-MD simulations, we employ Kohn-Sham DFT simulation techniques as implemented in the Vienna Ab initio Simulation

Package (VASP) [31] using the projector augmented-wave (PAW) method [32, 33], and molecular dynamics is performed in the NVT ensemble, regulated with a Nosé thermostat. Exchange-correlation effects are described using the Perdew, Burke, and Ernzerhof [34] (PBE) generalized gradient approximation (GGA). The pseudopotentials used in our DFT-MD calculations freeze the electrons of the 1s orbital, which leaves 10, 12, and 6 valence electrons for Mg, Si, and O atoms, respectively. Electronic wave functions are expanded in a plane-wave basis with an energy cut-off as high as 7000 eV in order to converge the total energy. Size convergence tests with up to a 65-atom simulation cell at temperatures of 10 000 K and above, indicate that pressures are converged to better than 0.6%, while internal energies are converged to better than 0.1%. We find, at temperatures above 500 000 K, that 15-atom supercells are sufficient to obtain converged results for both energy and pressure, since the kinetic energy far outweighs the interaction energy at such high temperatures [30, 35, 36]. The number of bands in each calculation was selected such that orbitals with occupation as low as 10^{-4} were included, which requires up to 14 000 bands in an 15-atom cell at 2×10^6 K and two-fold compression. All simulations are performed at the Γ point of the Brillouin zone, which is sufficient for high temperature fluids, converging total energy to better than 0.01% compared to a grid of k-points.

RESULTS

In Fig. 1, we show our EOS data points from Ref. [37] in temperature-density and temperature-pressure space. Computations were performed for a series of densities and temperatures, ranging from 6.42–64.16 g cm^{-3} and 10^4–10^7 K, respectively. To provide a guide for future ramp compression experiments, we also plot different isentropes, derived from the relationship $\frac{dT}{dV}\big|_S = -T \frac{dP}{dT}\big|_V / \frac{dE}{dT}\big|_V$ [27]. We find that the slope of the isentropes does not strongly depend on temperature, even though we compare conditions with differing degrees of ionization. Our results imply that the temperature rise with pressure along the isentropes approximately follows a power law, $T \propto P^\alpha$, with an exponent $\alpha = 0.309$ below 10^6 K, increasing only up to $\alpha = 0.399$ for temperatures above 10^7 K. This provides a simple rule for obtaining isentropic profiles in MgSiO$_3$ with wide-range validity, without the need of developing models for other properties of the material, such as the Mie–Grüneisen model.
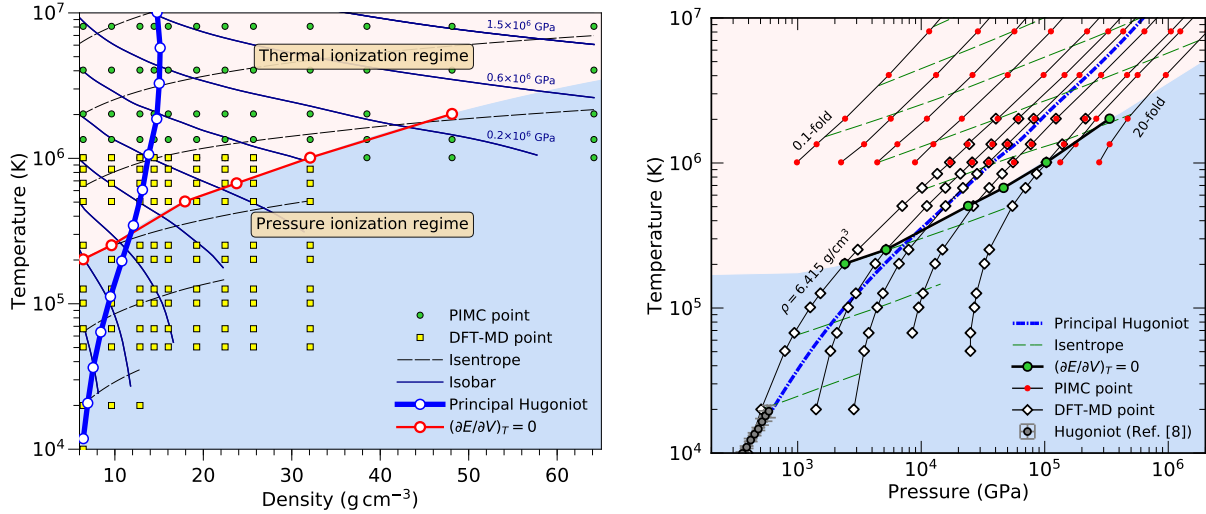

FIGURE 1. Conditions of our PIMC and DFT-MD and simulations along with computed isobars and isentropes. Densities from 0.1-fold (0.321 g cm^{-3}) to 20-fold (64.16 g cm^{-3}) and temperatures from 10^4–10^7 K were considered. The thick blue line shows the principal Hugoniot curve of MgSiO$_3$ derived from our simulations [37], using an initial density of $\rho_0 = 3.207911$ g cm^{-3} ($V_0 = 51.965073$ Å/f.u.).

The Hugoniot curve of MgSiO$_3$ obtained from shock experiments by Fratanduono *et al.* [8] is plotted along with our predicted Hugoniot curve on the temperature-pressure plot of Fig. 1. In the experiment, laser-driven shocks were used to compress enstatite up to 600 GPa, reaching temperatures as high as 2×10^4 K. This allowed to explore the solid and liquid regimes of MgSiO$_3$ and obtain a continuous measurement of the principal Hugoniot curve. We observe that our Hugoniot curve agrees very well with the experimental data.
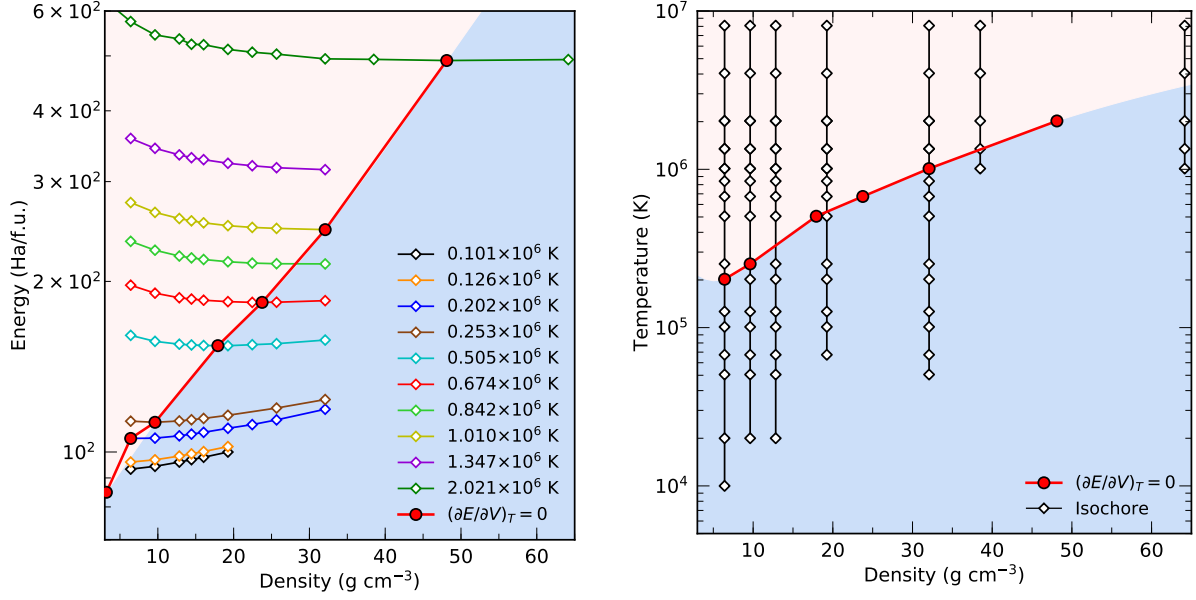
FIGURE 2. Left: Total energy of the MgSiO$_3$ system as a function of density along different isotherms. All energies have been shifted upwards by 800 Ha/f.u. in order to plot only positive energies on the logarithmic scale. The energy minimum on each isotherm, which satisfies the condition in Equation (4), is shown by the solid red circles. Right: MgSiO$_3$ isochores showing the same energy minima in the temperature-density space.

In Fig. 2, we plot the internal energy of the system at fixed temperature as a function of density. Most curves exhibit a minimum that satisfies the condition,

$$0 = \left.\frac{\partial E}{\partial V}\right|_T \equiv \left.\frac{\partial E}{\partial P}\right|_T \left.\frac{\partial P}{\partial V}\right|_T . \tag{1}$$

Because thermodynamic stability requires $\left.\frac{\partial P}{\partial V}\right|_T < 0$, this conditions is only satsified if $\left.\frac{\partial E}{\partial P}\right|_T = 0$. From the first law of thermodynamics, $dE = T\,dS - P\,dV$, it follows that

$$\left.\frac{\partial E}{\partial V}\right|_T = T\left.\frac{\partial S}{\partial V}\right|_T - P = T\left.\frac{\partial P}{\partial T}\right|_V - P, \tag{2}$$

where we have used the Maxwell identity $\left.\frac{\partial S}{\partial V}\right|_T = \left.\frac{\partial P}{\partial T}\right|_V$. Therefore, the condition in Equation (1) is satisfied if

$$0 = \left.\frac{\partial E}{\partial V}\right|_T = T\left[\left.\frac{\partial P}{\partial T}\right|_V - \frac{P}{T}\right] = T\left[\beta_V - \frac{P}{T}\right] = 0, \tag{3}$$

where $\beta_V \equiv \left.\frac{\partial P}{\partial T}\right|_V$ is the thermal pressure coefficient. Thus, the energy attains a mininum along an isotherm if the thermal pressure coefficient satisfies

$$\beta_V = \frac{P}{T} \ , \quad \text{or equivalently} \quad \left.\frac{\partial \ln P}{\partial \ln T}\right|_V = 1 \ . \tag{4}$$

We visualize this condition in the right panel of Fig. 3, where the dashed lines have a constant slope of 1 in the $\log(T)$-$\log(P)$ space.

For example, along the $T = 0.202 \times 10^6$ K isotherm shown in Fig. 2, we find an energy minimum around $\rho \approx 6.42$ g cm^{-3} while the slope $\left.\frac{\partial \ln P}{\partial \ln T}\right|_V$ becomes 1 at precisely the same temperature on the corresponding isochore, as we show
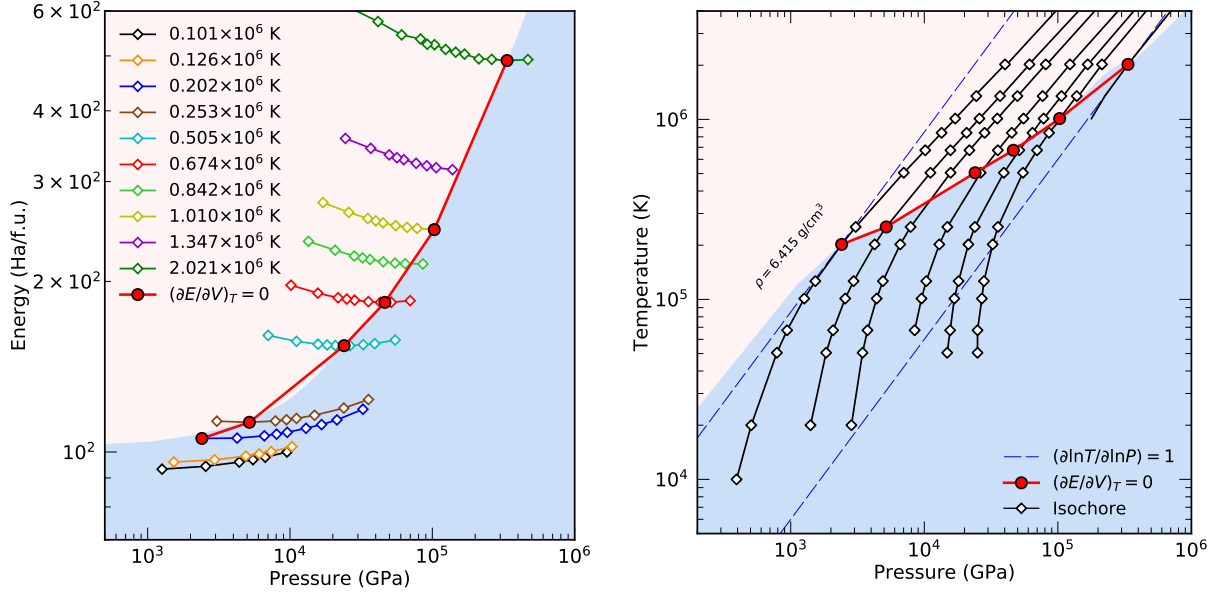
FIGURE 3. Left: Total energy of the MgSiO$_3$ system as a function of pressure along different isotherms. The energies have been shifted upwards by 800 Ha/f.u. in order to plot only positive energies in logarithmic scale. The energy minimum, which satisfies the condition in Equation (4), is shown by the solid red circles. Right: MgSiO$_3$ isochores showing the same energy minima in the pressure-temperature space, where condition (4) can be visualized. Two curves of slope equal to one in this $\log T$-$\log P$ plot are shown in dashed blue lines.

in Fig. 3. This slope descreases with increasing temperature, but at some point along the isochore this trend reverses and the slope starts to increase, converging asymptotically to 1 in the ideal gas limit at very high temperature. This condition is trivially fulfilled for an ideal gas, that satisfies $\left.\frac{\partial E}{\partial V}\right|_T = 0$ at any condition. At very high temperature, where all atomic species are completely ionized, we find that MgSiO$_3$ starts to behave like an ideal gas and the isochores approach a slope of 1. We confirm that this condition is satisfied in Fig. 1, that illustrates how all the isochores attain a slope of 1 at sufficiently high temperature.

From Equation (1) we infer that, if the energy attains a minimum as function of density it will also exhibit a corresponding minimum as a function of pressure, which we illustrate in the left panel of Fig. 3.

The degree of ionization is controlled by the statistical weights of free and bound states. In the limit of low density, where particles interact weakly, the internal energy increases with decreasing density because more and more free-particle states become accessible since their energies scale like $\rho^{2/3}$. Let us assume the energies of bound states do not change, which is reasonable in the weak-coupling limit. Under these assumptions, the degree of ionization and the internal energy will always increase if density is decreased at constant temperature. This regime is typically described well by the Saha equation [38] and we refer to conditions with $\left.\frac{\partial E}{\partial V}\right|_T > 0$ as the *thermal ionization regime*. Conversely, in the limit of high density, the internal energy increases with density and we refer to such conditions as the *pressure ionization regime*. Such an internal energy increase can only occur if the energy of the bound states increases. There may be several contributing factors including interaction and Pauli exclusion effects that modify the energy of bound but also of free states. In some cases, bound states merge with the continuum of free states. All these effects are expected to contribute to a rise in internal energy with increasing density, as we observed in our first-principles simulations at high density. We have shaded the thermal and pressure ionization regimes in the figures throughout this article. The condition in Equation (1) marks the boundary between the two regimes. From Fig. 4, we learn that the ionization of K shell electrons, that leads to a compression maximum along the shock Hugoniot curve, is a thermally driven process.

In the limit of low temperature, we expect the $\left.\frac{\partial E}{\partial V}\right|_T = 0$ line to converge to the density of ambient MgSiO$_3$ of $\rho_0 = 3.207911$ g cm^{-3}, which marks a minimum in internal energy. As any standard equation of state illustrates [39, 40], the internal energy of the solid will rise as the material is compressed or expanded without changing ionization
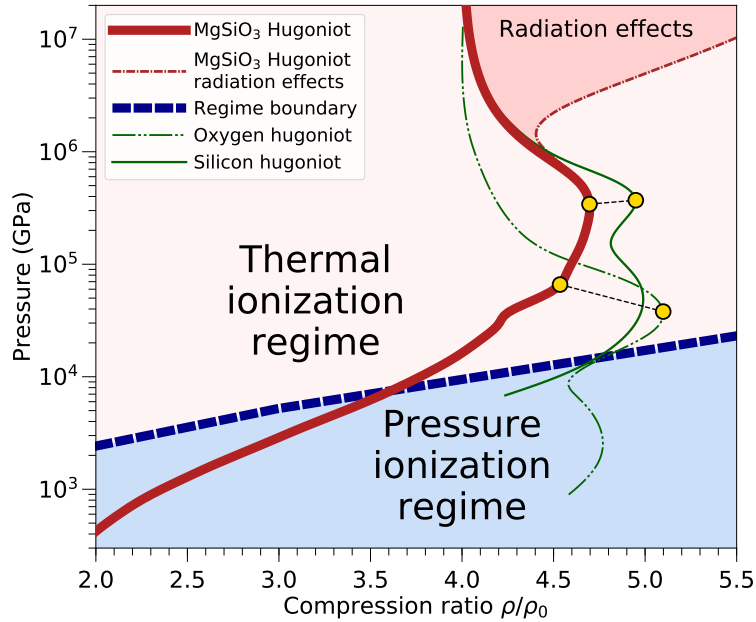
FIGURE 4. Comparison of the shock Hugoniot curve of $MgSiO_3$, oxygen [41], and silicon [17]. The thermal ionization of K shell electrons of Mg, Si, and O species leads to a broad maximum in compression. The lower and upper regions of this maximum can be associated with the corresponding compression maxima of pure oxygen and silicon.

state of the material. This is an example for an energy increase that is not associated with an noticible increase in the ionization fraction. In general, a density change will affect the energies of bound and free states if the system is strongly-coupled. It is only if the bound state energies are affected more severely that an increase in internal energy is associated with an increase in the degree of ionization. It is also possible that higher-lying bound states are affected by pressure ionization while lower-lying, confined states are not yet. Our energy criterion is not able to make such distinctions. Nevertheless, it detects increases in the energy of bound states, which is a necessary condition for pressure ionization to occur. So, in our view, this renders our energy criterion a useful approach to distinguish the regimes of thermal and pressure ionization.

CONCLUSION

We have constructed a consistent EOS of $MgSiO_3$ over a wide range of temperature and density conditions by combining results from DFT-MD and PIMC simulations in order to bridge the warm dense matter and plasma regimes [12, 42]. One goal of performing high-precision computer simulations based on first principles is to guide the design of inertial confinement fusion (ICF) experiments under conditions where the K and L shell electrons are gradually ionized, which is challenging to predict accurately with analytical EOS models.

Here we have introduced a simple thermodynamic criterion based on volume dependence of the internal energy that allows us to distinguish between the regimes of thermal ionization, $\frac{\partial E}{\partial V}\big|_T > 0$, and pressure ionization $\frac{\partial E}{\partial V}\big|_T < 0$. We conclude that the ionization of the K shell electrons is a thermally activated rather than pressure driven process under the condition where the compression maximum occurs on the principal shock Hugoniot curve.

ACKNOWLEDGMENTS

REFERENCES

1. F. Molster, T. Lim, R. Sylvester, L. Waters, M. Barlow, D. Beintema, M. Cohen, P. Cox, and B. Schmitt, "The complete ISO spectrum of NGC 6302," Astronomy & Astrophysics **372**, 165–172 (2001).

2. D. Valencia, M. Ikoma, T. Guillot, and N. Nettelmann, "Composition and fate of short-period super-Earths," Astronomy & Astrophysics **516**, A20 (2010).

3. R. M. Bolis, G. Morard, T. Vinci, A. Ravasio, E. Bambrink, M. Guarguaglini, M. Koenig, R. Musella, F. Remus, J. Bouchet, N. Ozaki, K. Miyanishi, T. Sekine, Y. Sakawa, T. Sano, R. Kodama, F. Guyot, and A. Benuzzi-Mounaix, "Decaying shock studies of phase transitions in MgO-SiO$_2$ systems: Implications for the super-Earths' interiors," Geophysical Research Letters **43**, 9475–9483 (2016).

4. S. Seager, M. Kuchner, C. A. Hier-Majumder, and B. Militzer, "Mass-Radius Relationships for Solid Exoplanets," The Astrophysical Journal **669**, 1279–1297 (2007).

5. D. Valencia, R. J. O'Connell, and D. D. Sasselov, "The role of high-pressure experiments on determining super-Earth properties," Astrophysics and Space Science **322**, 135–139 (2009).

6. F. W. Wagner, N. Tosi, F. Sohl, H. Rauer, and T. Spohn, "Rocky super-Earth interiors," Astronomy & Astrophysics **541**, A103 (2012).

7. F. González-Cataldo, S. Davis, and G. Gutiérrez, "Melting curve of SiO$_2$ at multimegabar pressures: implications for gas giants and super-Earths," Scientific Reports **6**, 26537 (2016).

8. D. E. Fratanduono, M. Millot, R. G. Kraus, D. K. Spaulding, G. W. Collins, P. M. Celliers, and J. H. Eggert, "Thermodynamic properties of MgSiO$_3$ at super-Earth mantle conditions," Phys. Rev. B **97**, 214105 (2018).

9. R. Kraus, S. Stewart, D. Swift, C. Bolme, R. Smith, S. Hamel, B. Hammel, D. Spaulding, D. Hicks, J. Eggert, *et al.*, "Shock vaporization of silica and the thermodynamics of planetary impact events," Journal of Geophysical Research: Planets **117** (2012).

10. J. Lindl, "Development of the indirect-drive approach to inertial confinement fusion and the target physics basis for ignition and gain," Physics of plasmas **2**, 3933–4024 (1995).

11. J. Gaffney, S. Hu, P. Arnault, A. Becker, L. Benedict, T. Boehly, P. Celliers, D. M. Ceperley, O. Čertík, J. Clérouin, *et al.*, "A review of equation-of-state models for inertial confinement fusion materials," High Energy Density Physics **28**, 7–24 (2018).

12. S. Zhang, A. Lazicki, B. Militzer, L. H. Yang, K. Caspersen, J. A. Gaffney, M. W. Däne, J. E. Pask, W. R. Johnson, A. Sharma, P. Surya-narayana, D. D. Johnson, A. V. Smirnov, P. A. Sterne, D. Erskine, R. A. London, F. Coppari, D. Swift, J. Nilsen, A. J. Nelson, and H. D. Whitley, "Equation of state of boron nitride combining computation, modeling, and experiment," Phys. Rev. B **99**, 165103 (2019).

13. D. K. Spaulding, R. S. McWilliams, R. Jeanloz, J. H. Eggert, P. M. Celliers, D. G. Hicks, G. W. Collins, and R. F. Smith, "Evidence for a Phase Transition in Silicate Melt at Extreme Pressure and Temperature Conditions," Phys. Rev. Lett. **108**, 065701 (2012).

14. F. Soubiran and B. Militzer, "Electrical conductivity and magnetic dynamos in magma oceans of Super-Earths," Nature Communications **9**, 3883 (2018).

15. D. M. Ceperley, "Path integrals in the theory of condensed helium," Rev. Mod. Phys. **67**, 279–355 (1995).

16. D. Ceperley, "Monte carlo and molecular dynamics of condensed matter systems," (Editrice Compositori, Bologna, Italy, 1996) p. 443.

17. B. Militzer and K. P. Driver, "Development of Path Integral Monte Carlo Simulations with Localized Nodal Surfaces for Second-Row Elements," Phys. Rev. Lett. **115**, 176403 (2015).

18. B. Militzer, E. L. Pollock, and D. Ceperley, "Path integral monte carlo calculation of the momentum distribution of the homogeneous electron gas at finite temperature," High Energy Density Physics **30**, 13–20 (2019).

19. R. Car and M. Parrinello, "Unified approach for molecular dynamics and density-functional theory," Phys. Rev. Lett. **55**, 2471–2474 (1985).

20. M. C. Payne, M. P. Teter, D. C. Allan, T. A. Arias, and J. D. Joannopoulos, "Iterative minimization techniques for ab initio total-energy calculations: molecular dynamics and conjugate gradients," Rev. Mod. Phys. **64**, 1045–1097 (1992).

21. D. Marx and J. Hutter, *Ab initio molecular dynamics: basic theory and advanced methods* (Cambridge University Press, 2009).

22. B. Militzer, W. Magro, and D. Ceperley, "Characterization of the state of hydrogen at high temperature and density," Contributions to Plasma Physics **39**, 151–154 (1999).

23. K. P. Driver and B. Militzer, "First-principles equation of state calculations of warm dense nitrogen," Phys. Rev. B **93**, 064101 (2016).

24. S. Zhang, B. Militzer, M. C. Gregor, K. Caspersen, L. H. Yang, J. Gaffney, T. Ogitsu, D. Swift, A. Lazicki, D. Erskine, R. A. London, P. M. Celliers, J. Nilsen, P. A. Sterne, and H. D. Whitley, "Theoretical and experimental investigation of the equation of state of boron plasmas," Phys. Rev. E **98**, 023205 (2018).

25. B. Militzer, *Path Integral Monte Carlo Simulations of Hot Dense Hydrogen*, Ph.D. thesis, University of Illinois at Urbana-Champaign (2000).

26. B. Militzer, D. M. Ceperley, J. D. Kress, J. D. Johnson, L. A. Collins, and S. Mazevet, "Calculation of a deuterium double shock hugoniot from ab initio simulations," Phys. Rev. Lett. **87**, 275502 (2001).

27. B. Militzer, "Path integral monte carlo and density functional molecular dynamics simulations of hot, dense helium," Phys. Rev. B **79**, 155105 (2009).

28. S. Zhang, K. P. Driver, F. Soubiran, and B. Militzer, "Equation of state and shock compression of warm dense sodium—A first-principles study," J. Chem. Phys. **146**, 074505 (2017).

29. K. P. Driver and B. Militzer, "First-principles simulations of warm dense lithium fluoride," Phys. Rev. E **95**, 043205 (2017).

30. K. P. Driver, F. Soubiran, and B. Militzer, "Path integral Monte Carlo simulations of warm dense aluminum," Phys. Rev. E **97**, 063207 (2018).

31. G. Kresse and J. Furthmüller, "Efficient iterative schemes for ab initio total-energy calculations using a plane-wave basis set," Phys. Rev. B **54**, 11169 (1996).

32. P. E. Blöchl, "Projector augmented-wave method," Phys. Rev. B **50**, 17953–17979 (1994).

33. G. Kresse and D. Joubert, "From ultrasoft pseudopotentials to the projector augmented-wave method," Phys. Rev. B **59**, 1758–1775 (1999).

34. J. P. Perdew, K. Burke, and M. Ernzerhof, "Generalized Gradient Approximation Made Simple," Phys. Rev. Lett. **77**, 3865–3868 (1996).

35. K. P. Driver and B. Militzer, "All-Electron Path Integral Monte Carlo Simulations of Warm Dense Matter: Application to Water and Carbon Plasmas," Phys. Rev. Lett. **108**, 115502 (2012).

36. K. P. Driver and B. Militzer, "First-principles simulations and shock Hugoniot calculations of warm dense neon," Phys. Rev. B **91**, 045103 (2015).

37. F. González-Cataldo, F. Soubiran, H. Peterson, and B. Militzer, "Path integral Monte Carlo and density functional molecular dynamics simulations of warm dense $MgSiO_3$," Physical Review B **101**, 024107 (2020).

38. W. Ebeling, W. Kraeft, and D. Kremp, *Theory of bound states and ionization equilibrium in plasmas and solids*, Ergebnisse der Plasmaphysik und der Gaselektronik, Band 5 (Akademie-Verlag, Berlin, 1976).

39. F. Birch, "Finite elastic strain of cubic crystals," Phys. Rev. **71**, 809–824 (1947).

40. P. Vinet, J. R. Smith, J. Ferrante, and J. H. Rose, "Temperature effects on the universal equation of state of solids," Phys. Rev. B **35**, 1945 (1987).

41. K. P. Driver, F. Soubiran, S. Zhang, and B. Militzer, "First-principles equation of state and electronic properties of warm dense oxygen," J. Chem. Phys. **143**, 164507 (2015).

42. S. Zhang, B. Militzer, L. X. Benedict, F. Soubiran, P. A. Sterne, and K. P. Driver, "Path integral Monte Carlo simulations of dense carbon-hydrogen plasmas," J. Chem. Phys. **148**, 102318 (2018).